Smart Materials and Structures

PAPER • **OPEN ACCESS**

Power-efficient piezoelectric fatigue measurement using long-range wireless sensor networks

To cite this article: David Rodenas-Herráiz *et al* 2019 *Smart Mater. Struct.* **28** 095004

OPEN ACCESS
IOP Publishing
Made open access 9 August 2019
Smart Materials and Structures
Smart Mater. Struct. **28** (2019) 095004 (17pp)
https://doi.org/10.1088/1361-665X/ab2c46

Power-efficient piezoelectric fatigue measurement using long-range wireless sensor networks

David Rodenas-Herráiz[1,3], **Xiaomin Xu**[1,3], **Paul R A Fidler**[1] and **Kenichi Soga**[2]

[1] Department of Engineering, University of Cambridge, Cambridge CB2 1PZ, United Kingdom
[2] Department of Civil and Environmental Engineering, University of California at Berkeley, Berkeley, CA, United States of America

E-mail: david.rodenas@eng.cam.ac.uk and xx787@cam.ac.uk

Received 12 April 2019, revised 20 May 2019
Accepted for publication 24 June 2019
Published 29 July 2019

Abstract

In this paper we describe the design of a proof-of-concept wireless embedded sensor system for continuous strain cycle monitoring as a method for fatigue life assessment on civil structures. Monitoring of strain cycles is energy demanding, and therefore not suited to energy-constrained devices, as it requires continuous acquisition of strain data with a high sampling rate, followed by data processing using algorithms for peak-trough detection and cycle counting. To overcome this drawback, at the core of our proposed design is a piezoelectric-based analogue sensor system that can achieve as much as a factor of 9 increase in energy efficiency compared with the conventional approach. The key component is an analogue peak-trough detector that offloads the computation in peak-trough detection from the microcontroller, thus eliminating the need for continuous sampling. The function of the detector is coupled with an energy-efficient interrupt-driven software design for acquisition and strain cycles calculation, which is carried out by using a standard form of the rainflow cycle counting algorithm. For wireless communication and networking, LoRa and LoRaWAN are adopted as core modules. We illustrate the performance of our proposed solution by way of simulation and laboratory experiments. Results show a good agreement in measurement of strain cycles between our proposed system and the conventional approach. Thus, our solution proves to be promising for real fatigue measurement applications.

Keywords: fatigue, strain cycles, PVDF, analogue peak-trough detector, interrupt-driven, rainflow cycle counting algorithm, LoRa

(Some figures may appear in colour only in the online journal)

1. Introduction

In situ monitoring of mechanical strain is important in the study of metal fatigue, where the objective is to understand the progressive failure and degradation mechanisms of civil structures like steel bridges, offshore platforms, cranes, lighting poles, gantries, or other high-profile engineering structures [1–5]. Although metal fatigue is a well-known engineering problem, its complete understanding remains a challenging and unsolved issue with much of the research looking at the effects of fatigue in steel bridges [3, 6–15]. Steel bridges are subjected to a large number of repetitive local strain concentrations of different magnitude caused mainly by vehicle loads. These cycling strain concentrations may lead to crack initiation and growth, corrosion, and eventual structural failure. The consequences of structural failure may come in many different forms, for example, material and structural damage, human injuries and fatalities, loss of the functionality of the structure and environmental damage. An example is the closure in November 2015 of the 55 year old Forth Road Bridge in Scotland because of a fatigue-induced crack found in the truss end linkage under the carriageway during a routine visual inspection [16]. The bridge

[3] Authors to whom any correspondence should be addressed.

was completely closed for three weeks with traffic restrictions imposed for several months while repairs were carried out, provoking major travel disruptions and a significant cost impact [17].

Several methods for assessing fatigue of civil structures have been proposed in the literature [18], which include non-destructuve testing (NDT) [19], piezoelectric actuators [6], acoustic emission [20], surface-mount piezoelectric paint sensors [21], vibration analysis [22], fibre Bragg grating sensing [23], and computer vision-based methods [24]. However, deployment cost and in most cases inability of these solutions to operate autonomously and/or remotely for long periods of time are key barriers to large-scale adoption in the civil engineering industry.

With merits of low cost sensing, ease of deployment and operation, and timeliness of data, wireless sensor networks (WSNs) have become a popular choice of remote instrumentation for civil engineering applications [25], including fatigue strain-cycle sensing [4, 7, 8, 12]. Two common approaches are wireless sensors that use either vibrating wire strain gauges (VWSGs) or conventional electrical resistance metal foil strain gauges. In either of these solutions, the conventional approach for monitoring fatigue strain cycles requires continuous data acquisition of strain by using a relatively high sampling frequency of the order of tens of Hz, which is necessary for achieving an effective strain cycles resolution [4, 12, 14, 24]. This draws substantial amounts of power, thus deeming VWSGs and electrical resistance strain gauges inappropriate for long-term monitoring unless compromises are made, such as wired power, high capacity, high voltage batteries (which may need regular replacement or recharging) or, if conditions are suitable, using energy harvesting techniques, e.g. a solar panel.

In this paper, we introduce an original design of a wireless sensor system for monitoring of fatigue strain cycles. Our design uses a piezoelectric transducer to sense mechanical strain continuously. A piezoelectric transducer is a device which generates an electrical signal proportional to the mechanical strain of the surface to which it is bonded. Unlike electrical resistance strain gauges, piezoelectric transducers do not need any external voltage excitation source in order to operate. In addition, research has shown that the major advantage of using piezoelectric sensors as opposed to electrical resistance strain gauges lies in their superior performance in terms of sensitivity, signal-to-noise ratio and high frequency noise rejection [26].

The key novelty of our proposed solution lies in the interaction between the built-in microcontroller (MCU) in the wireless platform and a custom-built analogue sensor system specifically designed for reducing sampling and computation workload at the MCU while minimising the power consumption of the whole system. As previously mentioned, the conventional approach for monitoring fatigue strain cycles requires continuous strain measurements at relatively high sampling frequencies. Acquired data are then processed by extracting the local maxima (peaks) and minima (troughs) and using such points to obtain strain cycles by way of a standard-based cycle counting method, such as the rainflow cycle counting algorithm [2, 27]. Finally, obtained strain cycles are grouped in the form of a histogram that reflects the number of strain cycles over the period of time covered by all the sampled data. For energy-constrained wireless devices, both sampling and computing tasks can demand excessive energy consumption, which adversely affects their operational lifetime and consequently the success and application of this solution.

To overcome this issue, our analogue sensor system design has the ability to detect peaks and troughs in the strain signal sensed by the piezoelectric transducer with no involvement of the MCU. The sought-after benefit of this approach is the elimination of the need for continuous data acquisition. Instead, the MCU remains in low-power energy saving mode most of the time and is only activated by our analogue sensor system to perform a single data acquisition of any detected peaks or troughs. Sampled peak/trough data are then processed by our embedded implementation of the rainflow cycle counting algorithm, and the results used to create and/or update a fatigue strain cycles histogram stored locally in our system. Finally, our solution is designed to transmit the generated histogram information using Long Range (LoRa) and LoRaWAN technologies, thus allowing for connectivity to other Internet of things (IoT) technologies [28].

Similar work—and also an example of a conventional system—by Bai *et al* [7] describes a piezoelectric-based wireless sensor system for local computation of fatigue strain characteristics using a digital signal processor. Although we were unable to compare our power consumption results with those of their experiments (not reported in their paper), we demonstrate experimentally that it is possible to offload from the processor in a uniprocessor system the computational burden of continuous data acquisition and peak-trough detection, achieving as a result as much as a factor of 9 reduction in power consumption while having a reasonable measurement accuracy.

Liu *et al* [13] designed a prototype of an NDT and piezoelectric-based wireless sensor for early detection of fatigue-induced cracks. The detection performance of their proposed solution is shown to be very promising both in the laboratory and by way of a case study on a real bridge structure. However, reported power consumption values are significantly higher (of the order of several hundreds of mW) than our results (5 mW on average). In fact, their design is intended to perform individual readings only once every week (or certain number of weeks), while our solution has the ability to sense continuously.

Finally, Alavi *et al* [9–11] presented a proof-of-concept wireless sensor and a data interpretation framework for early detection of distortion-induced fatigue cracks. The system is based on a self-powered piezo-floating-gate sensor, initially devised by Michigan State University for smart health monitoring of pavement systems [29]. Their approach consists of cumulatively measuring the duration of loading events whose strain level exceeds pre-selected levels. These measurements are stored internally and can only be retrieved by a service vehicle equipped with a radio frequency identification scanner. Our approach differs from the above in that we aim to recover the strain time series history by solely sampling peaks and troughs without any pre-defined thresholds and within the framework of long-term operation of low-power systems. In addition, our solution takes advantage of long-range wireless IoT technology for remote data retrieval.

1.1. Contributions

This paper makes three contributions:

- To our knowledge, this is the first attempt to apply the idea of a hardware-based peak-trough detection to applications such as fatigue strain-cycle monitoring that require continuous information about the times and/or amplitudes of the peaks and/or troughs in low frequency sensor signals. Our approach is supported by mathematical formulation, and can be validated both in simulation and experimentally.
- Through our hardware-based peak-trough detection approach, we leverage on-board computational capacity of energy-constrained data acquisition systems such as WSNs with the aim of reducing power consumption, and thus achieving a long operational lifetime. As such, we believe this paper both expands the scope of wireless IoT sensor systems and advances the field of fatigue monitoring and assessment.
- The paper also presents a study of the peak-trough detection accuracy achieved by our system by way of extensive computer simulations, followed by a system performance evaluation through laboratory experiments that compare our proposed solution with the conventional approach.

The remainder of this paper is organized as follows. Section 2 provides background on fatigue strain-cycle monitoring and analysis. Section 3 describes our solution, giving implementation details on the main hardware and software components. In section 4 we validate and show the performance of our system by way of simulation and laboratory experiments. Finally, section 5 concludes the paper.

2. Background on fatigue analysis

It is quite common for components of engineering structures to be subjected to repeated cyclic loads. These loads induce cyclic stresses within the material that result in microscopic physical damage, even when the gross stresses are well below the ultimate strength of the material. This microscopic damage accumulates over time as the cyclic stress continues until eventually a macroscopic crack or other visible damage appears. The process of permanent damage accumulation due to cyclic loading is known as fatigue.

While these discussions pertain to micromechanical processes, phenomenological continuum approaches are widely used to characterize the total fatigue life as a function of variables such as the applied stress range, strain range, mean stress and the environment. The fatigue life of a structure or a component is defined as the total number of cycles or time to induce fatigue damage and to initiate a dominant fatigue flaw which is propagated to final failure. The general view is that in a high-stress regime (commonly referred to as the low-cycle fatigue, LCF), fatigue life is primarily determined by crack propagation, whereas in a low-stress regime (referred to as the high-cycle fatigue, HCF), fatigue life is mainly dominated by crack initiation. This arbitrary division may vary from material to material depending upon its mechanical properties. From design viewpoint, the main concern for engineers is the high cycle region. However, low cycle fatigue data can be advantageous when only a short service life is required [1].

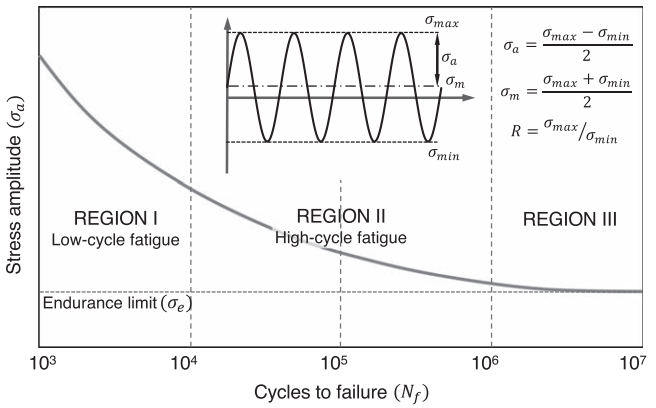

Figure 1. *S–N* curve, cyclic stress versus number of cycles to failure for fatigue characterisation.

2.1. S–N curve and fatigue limit of stress-life approach

The widely used stress-life approach in fatigue analysis was first introduced in the 1860s by Wöhler, mostly in HCF applications [2, 3]. This method is adopted in our research. The basis of the stress-life method is the Wöhler *S–N* diagram, as schematically shown in figure 1, which plots the nominal stress amplitude σ_a versus the number of cycles to failure N_f. It can be expressed as $\sigma_a = \sigma'_f(2N_f)^b$, where σ'_f and b are the fatigue strength coefficient and fatigue exponent, respectively. There are numerous testing procedures to generate the required data for a proper *S–N* diagram. *S–N* test data are usually displayed on a log–log plot, with the actual *S–N* line representing the mean of the data from several tests. Under constant amplitude loading conditions, the specimen under testing exhibits a plateau in the stress-life plot typically beyond about 10^6 fatigue cycles. Below this plateau level, the specimen may be cycled indefinitely without causing failure. This stress amplitude is known as the fatigue limit or endurance limit, σ_e, as indicated in figure 1. Definitions of other key terms include stress range $\Delta\sigma$ (the difference between the maximum stress and minimum stress), mean stress σ_m (the average of the maximum and minimum stresses), stress amplitude σ_a (half of the stress range), and stress ratio R (the ratio of minimum stress to maximum stress).

2.2. Mean stress effect

It is noted that most basic *S–N* fatigue data collected in the laboratory is generated using a fully-reversed stress cycle, where the mean stress of the fatigue cycle σ_m is zero ($R = -1$). However, this is not always representative of many applications. The mean level of the imposed fatigue cycle is known to play an important role in influencing the fatigue behaviour of engineering materials. To overcome this issue, one can apply the modified Goodman relationship, as expressed by:

$$\sigma_a = \sigma_{a|\sigma_m=0}\left(1 - \frac{\sigma_m}{\sigma_{TS}}\right), \quad (1)$$

where σ_a is the stress amplitude denoting the fatigue strength for a non-zero mean stress, $\sigma_{a|\sigma_m=0}$ is the stress amplitude for fully-reversed loading ($\sigma_m = 0$ and $R = -1$), and σ_{TS} is the tensile strength of the material.

2.3. Varying amplitude

The principles of stress-based characterization of total fatigue life are only relevant for constant amplitude fatigue loading. In reality, however, engineering components are invariably subjected to varying cyclic stress amplitudes, mean stresses and loading frequencies. A simple criterion for predicting the extent of fatigue damage induced by a particular block of constant amplitude cyclic stresses, in a loading sequence consisting of various blocks of different stress amplitudes, is provided by the so-called Palmgren–Miner cumulative damage rule [30]. Miner's rule states that the cumulative damage index, *CD*, is given by:

$$CD = \sum_i \frac{n_i}{N_i} = 1, \tag{2}$$

where n_i is the specified number of cycles for the ith stress range, S_i, and N_i is the corresponding number of cycles to failure for the ith stress range. This rule assumes that, when *CD* is equal to one, the cumulative damage should cause failure. Several structures design standards follow this methodology, such as the British Standard EN 1993-1-9 [31] and the American Association of State Highway and Transportation Officials (AASHTO) Bridge Design Specifications [32].

2.4. Strain monitoring and rainflow cycle counting

Prior to calculation of fatigue life, it is necessary to monitor strain over a significant period of time (of the order of days or even weeks). A cycle counting algorithm, such as the rainflow cycle counting algorithm [27], is then used to process the strain time series and extract a stress range histogram. A stress range histogram presents the occurrence of stress cycles in terms of the number of cycles for each stress range magnitude captured during the measurement period. Then, this variable amplitude loading in the histogram is converted to an effective constant amplitude stress cycle using Miner's rule. This effective stress is used to calculate the total number of cycles that the structural (or mechanical) component could experience through all its lifetime by using the aforementioned *S–N* curves. Finally, the total number of cycles to failure is converted to the remaining lifetime in years.

The authors are aware of a number of sources of uncertainty in the analysis of fatigue results, in general, and in the use of the stress-life approach, including the estimation of material properties, service conditions and environment. Such uncertainties could be analysed using known statistical approaches to derive the level of reliability or probability of failure. These factors are beyond the scope of the current work, but will be considered in future analytical work on fatigue data captured using our proposed approach.

Other commonly used methods are the strain-life and the fracture mechanics methods. The strain-life method is used for the study of the process of crack initiation, whereas the fracture mechanics method is used for the study of crack propagation mechanisms over time. The latter may be combined with the strain-life method in order to consider crack initiation.

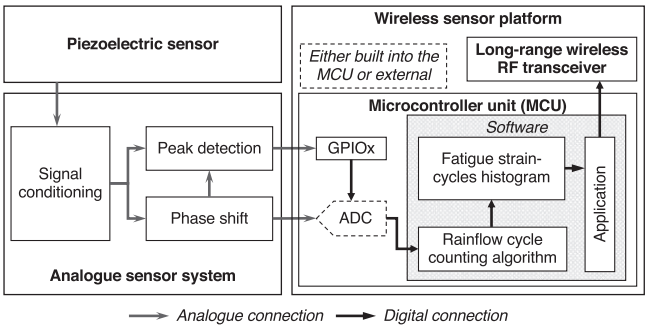

Figure 2. System overview.

3. Proposed architectural design

Figure 2 shows the block diagram of our proposed wireless sensor system for fatigue strain-cycles monitoring consisting of three distinct components: a piezoelectric transducer, an analogue sensor system, and a wireless sensor platform. The piezoelectric sensor is to be attached to a structural element where fatigue damage is likely to occur. At this attachment point, any mechanical strain would be converted by the piezoelectric sensor into an alternating current (AC), and passed through the analogue sensor system. The analogue sensor system converts the output current from the sensor into a measurable voltage signal, and then generates a hardware interrupt whenever it detects a peak or trough (local maximum or minimum) in such voltage signal. For every signal interrupt, the MCU embedded in the wireless sensor platform triggers an analogue-to-digital converter (ADC) reading. The measured data point is input to the rainflow cycle counting algorithm [27]. Results from the algorithm are used to create and/or update a histogram that represents the cumulative strain distribution over time.

The final step is the wireless transmission of the generated histogram information. The transmission interval is application-specific, e.g. hourly, daily or even weekly. In our work, wireless communication and networking are based on *Lo*ng *Ra*nge (LoRa) and LoRaWAN [33], respectively, but other wireless technologies, such as Narrowband IoT (NB-IoT) [34], may be adopted. LoRa is a proprietary radio modulation technology developed by Semtech Corporation. LoRa has become the underlying physical layer technology proposed for use in LoRaWAN, an open-source PHY and MAC protocol stack actively supported by the LoRa Alliance. Compared to other low-power wireless systems (e.g. IEEE 802.15.4-based radios), LoRa brings many sought-after benefits for outdoor monitoring applications, which include: longer communication range (of the order of several km in rural areas) with similar power consumption, increased robustness against interference and noise, and higher multipath, fading and Doppler resistance [35].

In the following subsections, we describe each component in detail.

3.1. Piezoelectric thin film sensor

The fundamental operating principle of piezoelectric materials is that they generate an electrical charge or electrical polarization in response to an external force, i.e. a mechanical stress. This phenomenon is known as the *direct piezoelectric effect*. When the material is compressed, it creates a charge of the same polarity as the polar axis. When the force is reversed, i.e., the material is stretched, it outputs a charge of opposite polarity. Thus, a reciprocating mechanical force results in an alternating output current, whose amplitude and frequency are directly proportional to the mechanical deformation of the material. There is also a converse effect, called the *indirect piezoelectric effect*, whereby an applied electrical field produces a proportional deformation of the material. For measuring strain, we take advantage of the direct piezoelectric effect.

From the electrical point of view, a piezoelectric ceramic thin film sensor, such as a Polyvinylidene fluoride (PVDF)-based sensor, can be modelled by two types of equivalent circuits: either a current source in parallel with a capacitance, or a voltage source in series with a capacitance. As shown in figure 3(a), we choose to use the second circuit type consisting of a voltage source, v_p, representing the induced voltage across the sensor terminals, and a series capacitance, C_p, indicating the capacitance of the film. In such model, we also consider a capacitance C_c in parallel with v_p, to model the capacitance of the cables which carry the output signal of the sensor. The v_p is related to C_p and the charge generated by the film sensor, q, as $v_p = q/C_p$.

The mathematical expression of the generated charge q can be found by integrating the electrical displacement, D, over the area of the film, A_p ($=l_p b_p$, where l_p and b_p are the length and width of the film, respectively), as $v_p = \iint_{A_p} D\, \mathrm{d}A_p$, where d is the coefficient of proportionality. Rigorous definitions of the electrical displacement and the coefficient of proportionality, as well as their relation to the strain ε may be found elsewhere [26, 37]. Considering the effects of longitudinal (1-direction) and transverse (2-direction) strains, the actual definition of the electrical displacement is $D = d_{31} Y_{11} \varepsilon_1 + d_{32} Y_{22} \varepsilon_2$, where $Y \approx Y_{11} \approx Y_{22}$ is the Young's modulus of the piezoelectric material. For a longitudinal stress, there will be a lateral strain due to the Poisson's effect at the location of the sensor, such that $\varepsilon_2 = -\nu\varepsilon_1$, where ν is the Poisson's ratio of the material to which the sensor is attached (typically 0.2 for steel). To account for the Poisson's effect in the total strain, a correction factor K_p may be applied. For PVDF, this correction factor is $K_p = (1 - \nu d_{31}/d_{32})$.

Shear lag effects caused by finite thickness bond may also be accounted for by way of the derivation of another correction factor K_b. The value of K_b is dependent only on the geometry of the sensor. For PVDF, it has been shown that K_b is very close to unity and therefore the shear lag effect could be neglected [26].

The relation between the strain and voltage generated by the sensor, considering the Poisson's and shear lag effects, is given by the equation (3). In this equation, $S_q = d_{31} Y_{11} A_p$ is defined as a sensitivity parameter, whereas the capacitance C_p is given by $C_p = \varepsilon_0 \varepsilon_r A_p / t_p$, where t_p is the thickness of the sensor, ε_0 is the vacuum permittivity and ε_r is the relative permittivity of the piezoelectric material.

$$\varepsilon = \frac{v_p C_p}{S_q K_p K_b}. \tag{3}$$

Piezoelectric sensors have typically a very high output impedance that results in a very small electrical charge, which is difficult to measure using ordinary oscilloscopes and voltmeters. To measure v_p the output signal of the piezoelectric sensor needs

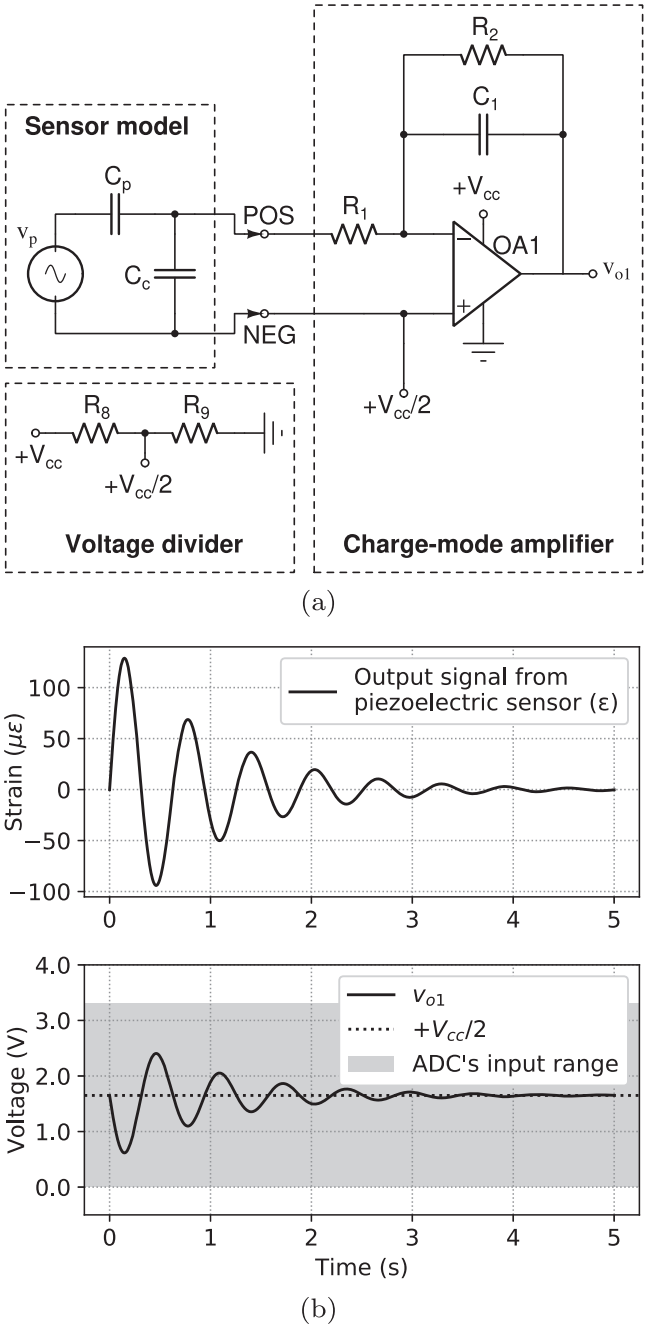

Figure 3. Sensor signal conditioning: (a) equivalent electrical circuit; (b) example of operation, where the top side shows the sensor's output and the bottom side the output from the signal conditioning circuit. For this example, the sensor model is based on the PVDF sensor DT1-028K from TE Connectivity [36], $C_1 = 4\mathrm{nF}$, $R_2 = 1G\Omega$ and $V_{cc} = 3.3V$. Conversion from strain to voltage output, and vice versa, is based on equation (4).

to be passed through some signal conditioning electronics with sufficient high impedance (of the order of $M\Omega$ or even $G\Omega$) in its input and low impedance in its output. With this configuration, it is possible to produce an output voltage that is large enough to be measured with most ADCs. Details of the signal conditioning design used in this work are given below.

3.2. Analogue sensor system

Our analogue sensor system design has one input, i.e. the AC current output signal from the piezoelectric film, and two outputs: (i) a hardware interrupt to signal the occurrence of peaks and troughs, and (ii) a voltage signal that is proportional to the current signal of the piezoelectric sensor and that can be measured using an ADC The two main building blocks of our analogue sensor system are signal conditioning and peak-trough detection. The first block allows matching of the output impedance and range of the piezoelectric film to the input impedance and measurement range requirements of the ADC that is to be used, while the second building block implements our analogue circuit design for continuous peak-trough detection. Please note that, in our wireless sensor system design, we consider the ADC to be part of the wireless sensor platform rather than being integrated into the analogue sensor system itself, such that the dimensions and power requirements of the system are kept to a minimum. An additional benefit of this approach is that our design can be easily interfaced with any MCU with an on-chip ADC, such as the ARM Cortex-M3-based MCUs, which are becoming commonplace in most IoT low-power embedded systems. In this work, we use the *NZ32-L151* platform from Modtronix Engineering [38], which uses the ST Microelectronics ARM Cortex-M3-based STM32L151RC MCU featuring a 12 bit successive-approximation-register (SAR) ADC, but other MCU chips and/or ADC types could be adopted.

3.2.1. Signal conditioning stage. The circuit shown in figure 3(a) represents the input signal conditioning for the piezoelectric film sensor. The circuit collects the charge input signal from the film and produces a measurable voltage that is proportional to the input charge.

To be able to convert the input current from the film, a charge-mode amplifier is used. The charge-mode amplifier consists of an operational amplifier ('op-amp' for short) (component OA1 in the figure), with a negative feedback loop based on a feedback resistor (R_2) and a feedback capacitor (C_1) in parallel. The op-amp is required to have a high input resistance and low bias current. The former avoids bleed-off of the charge on the feedback capacitor, while the latter prevents the capacitor from charging and discharging at excessive rates [39]. LPV811 [40] from Texas Instruments is a single-supply op-amp with nano-current consumption (~450 nA) that fulfils these requirements and is chosen for this circuit. The resistor R_1 is also added in series with the op-amp inverting input to improve the stability of the circuit and further increase its input resistance by limiting input currents due to accidental high input voltage [41]. On the other hand, the output voltage of the charge-mode amplifier, v_{o1}, is shifted to the middle of the input range of the ADC by using a DC reference voltage. This reference voltage is equal to half of the input supply voltage, i.e. $+V_{cc}/2$, which is obtained by halving the input supply voltage using a voltage divider (resistors R_8 and R_9). Note that the circuit design, which also includes the peak-trough detection and sampling stages described later, allows single supply operation. In our design, the supply source is taken from the same power source as the wireless platform. Figure 3(b) illustrates an example of operation.

From [26, 41], the output voltage of the charge amplifier can be derived as:

$$v_{o1} = \frac{+V_{cc}}{2} - \left(\frac{j\omega R_2 C_1}{1 + j\omega R_2 C_1}\right)\frac{S_q \varepsilon}{C_1} = \frac{+V_{cc}}{2} - H(jw)\left(\frac{S_q \varepsilon}{C_1}\right), \quad (4)$$

where $H(jw)$ is the complex transfer function of the charge amplifier and ω is the angular frequency of operation. One important advantage of the charge amplifier circuit is that its transfer function, and hence its output, are neither affected by the capacitance of the film C_p nor of the connecting cable C_c. This fact is reflected in equation (4). As seen, the output of the circuit depends only on the value of the feedback capacitor C_1. Thus, with the appropriate choice of C_1 (while assuming a fixed value of the feedback resistance R_2) it is possible to adjust the sensitivity of the circuit and provide the required measurement range. However, it is to be noted that the circuit exhibits a low cut-off frequency, $f_l^H = 1/(2\pi R_2 C_1)$. As stated in [26], this sets a design trade-off between the achievable sensitivity and the values that can be selected for R_2 and C_1 mainly due to operational constraints.

3.2.2. Peak detection and sampling stages. Our proposed peak-trough detector consists of a non-inverting op-amp comparator with positive feedback, also called non-inverting Schmitt trigger, and a linear resistor-capacitor (RC) delay circuit connected to the inverting input terminal of the op-amp comparator. Figure 4(a) (top) shows the equivalent electrical circuit. The basic functionality of the op-amp comparator (op-amp OA2 in the figure) is to compare two input analogue signals (one at each op-amp's input terminal) and give a binary output signal as a result of the comparison. The output signal v_{o2} has two possible levels, V_{OH} and V_{OL} (where $V_{OH} > V_{OL}$), representing the high-level and low-level outputs of the comparator, respectively. The circuit requires a rail-to-rail op-amp such that its output swings closer to the positive ($V_{OH} \approx +V_{cc}$) and negative ($V_{OL} \approx V_{ee}$; in our design V_{ee} is tied to ground) rails, and thus output state transitions can be better identified and used to trigger hardware interrupts. OPA333 [42] from Texas Instruments is a fast rail-to-rail, single-supply op-amp with micro-current consumption and is chosen for both op-amps OA2 and OA3 in figure 4(a).

The operation of the circuit is as follows. The analogue output signal from the charge amplifier circuit v_{o1} is applied to the non-inverting terminal of the op-amp comparator. The same signal v_{o1} is also applied to the RC delay circuit formed by the resistor R_5 and the capacitor C_2. The output signal, that we denote as v_{o1}^{ϕ}, lags behind v_{o1} in phase, and is applied to the

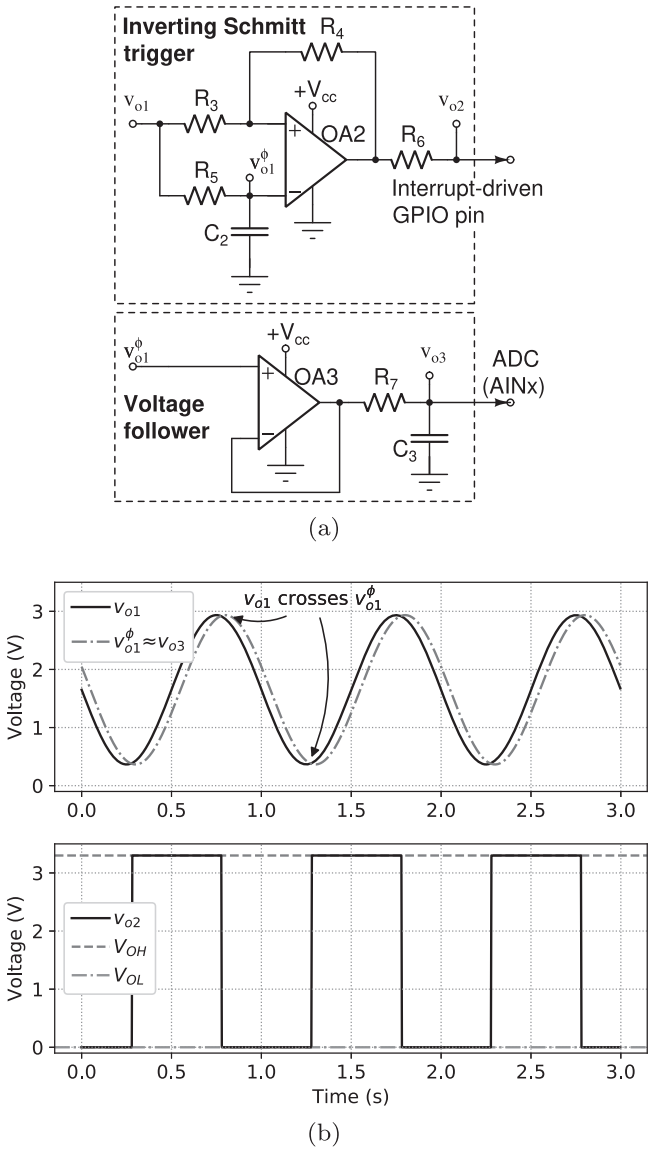

Figure 4. Peak-trough detection: (a) equivalent electrical circuit; (b) example of operation, where the top side shows the input to the op-amp OA2, i.e. v_{o1} and v_{o1}^{ϕ}, and the bottom side the output signal v_{o2}, resulting from comparing v_{o1} and v_{o1}^{ϕ}. For this example, the two possible states of v_{o2} depend on the supply voltage for the op-amp OA2, i.e. $V_{\mathrm{OH}} = +V_{cc} = 3.3$ V while $V_{\mathrm{OL}} = V_{ee} = 0$ V.

inverting terminal of the op-amp. The signal v_{o2} results from the comparison between v_{o1} and v_{o1}^{ϕ}. Transitions from low to high and high to low are used to signal the occurrence of a peak or trough, respectively. For every transition, an interrupt to the MCU followed by a single ADC conversion of the signal v_{o3} is generated. The signal v_{o3} is effectively v_{o1}^{ϕ} after being passed through a buffer amplifier, also called voltage follower (op-amp OA3). The buffer amplifier is used to avoid loading effects arising from the direct connection of v_{o1}^{ϕ} to the ADC, which can significantly affect the reliability of the peak-trough detection. A single-pole low-pass RC filter (R_7/C_3) follows the buffer amplifier to further reduce out-of-band noise.

It is important to note that the series RC delay circuit in our design is in fact another first-order low-pass filter, with cut-off frequency:

$$f_l^F = \frac{1}{(2\pi R_5 C_2)} \tag{5}$$

and no signal gain. This has the following two implications. First, the circuit only passes unaltered low frequency signals from 0 Hz to its cut-off frequency, while attenuating or weakening others. This means that R_5 and C_2 must be appropriately chosen such that those frequencies of interest to fatigue strain monitoring (typically from 1 to 20 Hz [4, 7, 14, 15, 24, 29]) pass through the RC circuit unaffected. Second, as the filter contains a capacitor, there exists a lagging phase difference between v_{o1} and v_{o1}^{ϕ} determined by $\phi = -\arctan(2\pi f_{v_{o1}} R_5 C_2)$, where $f_{v_{o1}}$ is the signal frequency of v_{o1}. This phase lag is important in our case to find peaks and troughs. The op-amp looks at any voltage value of v_{o1} and compares it with the voltage level at v_{o1}^{ϕ}, which corresponds to an earlier level of v_{o1}. Thus, we can determine whether the polarity of slope of v_{o1} is either positive (i.e. the signal voltage is increasing thus approaching to a peak), negative (i.e. the signal voltage is decreasing thus approaching to a trough), or whether the polarity changes (a peak or trough has been reached). One disadvantage of this circuit is that the phase lag is not constant over the range of frequencies of v_{o1}, being smaller at lower values. Nonetheless, with the appropriate choice of R_5 and C_2, it is possible to design an RC circuit with the desired phase lag at the sensor signal frequencies of monitoring interest. The impact of selection of R_5 and C_2 on performance is discussed in section 4.

We next describe the operation of our peak-trough detector circuit analytically [43]. The comparator's output signal v_{o2} is given by:

$$v_{o2} = A_{\mathrm{OA2}}(v_+ - v_-), \tag{6}$$

where v_+ and v_- are the voltage signals at the non-inverting and the inverting terminals, respectively, and A_{OA2} is the circuit's gain.

The signal v_+ at the non-inverting terminal is a combination of the op-amp's output v_{o2}, its input v_{o1}, and the voltage divider formed by resistors R_3 and R_4:

$$v_+ = v_{o1}\frac{R_4}{R_3 + R_4} + v_{o2}\frac{R_3}{R_3 + R_4}. \tag{7}$$

The signal v_- at the inverting terminal corresponds to the voltage output of the preceding passive low-pass RC filter, v_{o1}^{ϕ}. The governing equation for v_{o1}^{ϕ} can be found to be [44]:

$$v_{o1}^{\phi} = \left(\frac{1}{1 + j\omega R_5 C_2}\right) v_{o1} = F(j\omega) v_{o1}, \tag{8}$$

where $F(j\omega)$ is the transfer function of the RC filter.

From expression 6, we see that the transitions will occur when v_+ crosses v_{o1}^{ϕ}, then:

$$v_{o1}^{\phi} = V_{T_{\rightarrow}}\frac{R_4}{R_3 + R_4} + v_{o2}\frac{R_3}{R_3 + R_4}, \tag{9}$$

where $V_{T_{\rightarrow}}$ is the transition voltage. From [43], the transition voltage from V_{OH} to V_{OL}, and vice versa, can be derived,

respectively, as:

$$V_{T_{\mathrm{OH}\to\mathrm{OL}}} = V_s - V_{\mathrm{OH}}\frac{R_3}{R_4}, \tag{10a}$$

$$V_{T_{\mathrm{OL}\to\mathrm{OH}}} = V_s - V_{\mathrm{OL}}\frac{R_3}{R_4}, \tag{10b}$$

where $V_s = v_{o1}^{\phi}(1 + R_3/R_4)$.

The non-inverting Schmitt trigger circuit inherently exhibits hysteresis, which depends on the values for resistors R_3 and R_4 (equation (11)) but also on the frequency of the input signal v_{o1}. This characteristic can be used to ignore any noise introduced in v_{o1}, as well as very small peak-to-peak strain signals with limited or no contribution to fatigue strain-range calculation. This has an advantage that interrupt triggers for sampling and subsequent strain range cycle computation, and hence the overall power consumption, can be further reduced.

$$V_{hyst} = V_{T_{\mathrm{OL}\to\mathrm{OH}}} - V_{T_{\mathrm{OH}\to\mathrm{OL}}} = (V_{\mathrm{OH}} - V_{\mathrm{OL}})\frac{R_3}{R_4}. \tag{11}$$

Figure 4(b) illustrates an example of the operation of our peak-trough detector circuit. For ease of explanation, let us assume that the voltage levels of v_{o1} and v_{o1}^{ϕ} are both increasing and thus approaching a peak. As seen, in this case the polarity of the slope of v_{o1} is positive. In addition, the op-amp comparator's output v_{o2} is at its high voltage state, V_{OH}, and will remain at this state as long as the voltage of both signals is the same. At the moment in time where the voltage of v_{o1} reaches its peak and starts decreasing towards the next trough, the voltage level of v_{o1}^{ϕ} is still increasing. When v_{o1} crosses v_{o1}^{ϕ}, the op-amp immediately changes its output from high to low (i.e. from V_{OH} to V_{OL}). Shortly after, v_{o1}^{ϕ} is also at its peak value and starts decreasing. The voltages of both signals are now the same and therefore the op-amp's output remains at its low state. The same reasoning, in reverse, applies to the occurrence of a trough.

3.3. Software architecture

We designed the software architecture to be easily extendable to other embedded platforms that may be programmed with a C-based operating system (OS) such as Contiki OS [45] or freeRTOS [46]. In our work, all software modules including the firmware for the NZ32-L151 platform and the LoRa transceiver module used (i.e. SX1276-based module also from Modtronix Engineering), as well as the LoRaWAN endpoint protocol stack [47], were implemented and/or ported for the Contiki OS. Source code is available online [48].

Data acquisition and wireless transmission tasks are executed in an interrupt-driven manner. Data acquisition is primarily triggered by external interrupts from the analogue sensor system, whereas wireless transmission may be triggered by internal interrupts generated by the running application. For data acquisition, the GPIO line connected to the output signal v_{o2} of the analogue sensor system is set as input to the MCU and configured to detect changes in v_{o2} from low to high (trough) and from high to low (peak). In this way, an interrupt to the MCU is generated when a peak or trough occurs. This interrupt wakes up the MCU from low-power mode (we use the *stop* mode in our implementation [49]) and then triggers the acquisition of a single data point using the MCU's built-in ADC The acquired data point is stored in a buffer in the RAM memory for later analysis by using the rainflow cycle counting algorithm. Such analysis will be carried out when the buffer is full. Results from the algorithm will then be grouped in the form of a histogram that will be updated as new results are obtained. Finally, the MCU is allowed to go into low-power mode to save energy when there are neither any interrupt calls to be serviced nor any computation tasks in progress.

Details of the rainflow cycle counting algorithm are given next.

3.3.1. The rainflow cycle counting algorithm. Our implementation of the rainflow cycle counting algorithm is based on the three-point algorithm presented by Bannantine *et al* [2]. However, our implementation differs from Bannantine *et al* in that no re-arrangement of the series of peaks and troughs is necessary prior to analysis. Our implementation also differs in that it requires an extra point to be considered at each iteration of the algorithm in order to discern between one-half and full cycles, as described in section 5.4.4 of the ASTM E1049-85 standard [27].

In each iteration, a sequence $s[\,]$ containing the three most recently acquired consecutive points in the series of peaks and troughs S (i.e. the buffer stored in the RAM memory) is analysed. The storage data size of S is limited to a vector length of N_S values in order to minimise memory overheads of the algorithm. The parameter N_S can be configured at compile time (as a power of two) and is specific to the deployment in which the wireless sensor system is used. Each iteration of the algorithm involves comparing the magnitude of two strain ranges X_n and Y_n formed by the sequential strain values $s[n-2, n-1, n]$, such that

$$\begin{aligned} X_n &= |s[n] - s[n-1]| \\ Y_n &= X_{n-1} = |s[n-1] - s[n-2]|, \end{aligned} \tag{12}$$

where n is an index to the series S. As aforementioned, our implementation requires an extra point K, which is always the first element in the series. A cycle is identified if $X_n \geqslant Y_n$, being Y_n its strain range. If the sequence s contains K (i.e. $K = s[n-2]$), the cycle is counted as a one-half cycle; otherwise, the cycle is a full cycle. For each one-half cycle, the point $K = s[n-2]$ is removed from the series, in which case K points to $s[n-1]$ and the algorithm proceeds, in a similar manner, with the sequence of three points $s[n-1, n, n+1]$. Conversely for each full cycle, the points $s[n-2]$ and $s[n-1]$ are removed from the series, and the algorithm proceeds with the sequence $s[n-4, n-3, n]$. If no cycle is identified, then the next iteration of the algorithm considers the sequence $s[n-1, n, n+1]$ and so on until the entire series is processed. Our implementation of the rainflow cycle counting algorithm runs in $O(N_S)$ time and requires $O(N_S)$ space. Algorithm 1 shows the pseudo-code of our implementation of the rainflow cycle counting algorithm.

Algorithm 1. Rainflow cycle counting algorithm

Initialization : Set three-point sequence $s = \{0\}$, $n = 0$, $K = 0$
Data: Vector S containing peaks and troughs
1 **if** *(At the end of S)* **then**
  Go to 6;
else
  Assign next peak or trough from S to s, $n = n + 1$;
  Set K to point to the first element in S;
2 **if** $(n < 3)$ **then**
  Go to 1;
else
  $X_n = |s[n] - s[n-1]|$;
  $Y_n = |s[n-1] - s[n-2]|$;
3 **if** $(X_n \geqslant Y_n)$ **then**
  Go to 4;
else
  Go to 1;
4 **if** $(K \subset Y_n)$ **then**
  Go to 5;
else
  Store Y_n as one cycle for later histogram creation/update;
  Remove $s[n-2, n-1]$ from S so that s only contains $s[n]$, $n = n - 2$;
  Go to 2;
5 Store Y_n as one-half cycle for later histogram creation/update;
Remove $s[n-2]$ from S so that s only contains $s[n-1, n]$, $n = n - 1$;
Go to 2;
6 Store each range that has not been previously counted as one-half cycle, then STOP;

3.3.2. Histogram representation and wireless transmission of strain cycles. A histogram with equally sized bins is constructed and continuously updated with the strain cycle values computed using the rainflow cycle counting algorithm. More specifically, we build and maintain two unsigned 32 bit integer arrays, one per each cycle type, that map from a strain range interval to its associated number of cycles. This allows us to count up to $2^{32} - 1$ strain cycles per bin, or equivalently, per strain range interval. Given a cycle with strain range r_ε, we find the bin i it belongs to by dividing r_ε by the histogram's bin width. This approach has $O(1)$ runtime performance and requires $O(nbins)$ space, where *nbins* is the number of bins or strain range intervals in the histogram.

The lower and upper range values (minimum and maximum strain range values of monitoring interest) of the histogram, as well as the bin width are application-specific parameters and should be chosen such that the distribution of strain cycles over any desired period of time (e.g. an hour, a day or a week) can be observed clearly from the histogram. In particular, cycles with a strain range falling below the lower bound of the histogram are discarded and hence not transmitted via wireless. This lower bound may be chosen simply by applying engineering judgement based on prior knowledge of the strain ranges that are typically encountered in the monitored asset, including their relevance to potential fatigue damage. Our current software implementation allows specification of these parameters only at compile time. Future work considers providing support for over-the-air parameter configuration to adapt to potential changing strain conditions over time as well as to civil engineer(s) requirements for strain data collection and information processing.

An important choice to make is the number of histogram bins. A trade-off exists between this and the maximum possible data payload of a LoRa/LoRaWAN data frame, which in turns depends on the selected transceiver settings. These settings include the modulation type (i.e. either LoRa or frequency-shift keying (FSK) modulation), carrier frequency, transmit power, spreading factor, coding rate and channel bandwidth. Selection of these parameters can be made to meet end application requirements, but the link between these poses an important performance-related trade-off between transmission throughput, energy consumption, communication range and resilience to noise [50]. Therefore, if the application message size, which is dependent on the number of histogram bins, exceeds the maximum available data payload in the resulting LoRa data frame, more transmissions are required in order to send the entire histogram. This choice can lead to increased energy consumption, possibly compromising operational lifetime where the power source relies on the sole use of batteries.

4. Results

In this section we use extensive computer simulation and laboratory experiments on real hardware to validate our proposed solution. All the simulation scripts, the scripts for data analysis, and the generated simulation and experimental data are available online [48].

4.1. Simulation: evaluation of detection performance

An important consideration in the operation of our proposed system is the inherent short time lag that exists between when a signal peak (or trough) occurs and when the ADC obtains the subsequent strain reading from the signal v_{o3}. The first source of lag is in the peak-trough detection since peaks and troughs are signalled shortly after the actual points occur. Lags in the electronics, interrupt latency and the latency and settling time of the ADC also add to the total time lag. The above adversely affects the detection performance of our system in terms of measurement accuracy, which is defined as the closeness of the measured value to the true value of the signal peak or trough. Therefore, our initial objective is to evaluate the detection performance of our system and the influence of choosing different hardware components, such as the resistances R_3 and R_5 and the capacitance C_2, on the measurement accuracy.

While the operation of the entire analogue sensor system including signal conditioning can be simulated at once, in this part we only consider the peak-trough detector circuit. We do so in order to have full control of the characteristics (i.e. signal amplitude and frequency) of the signal v_{o1} that is input to the circuit. The evaluation is performed using extensive

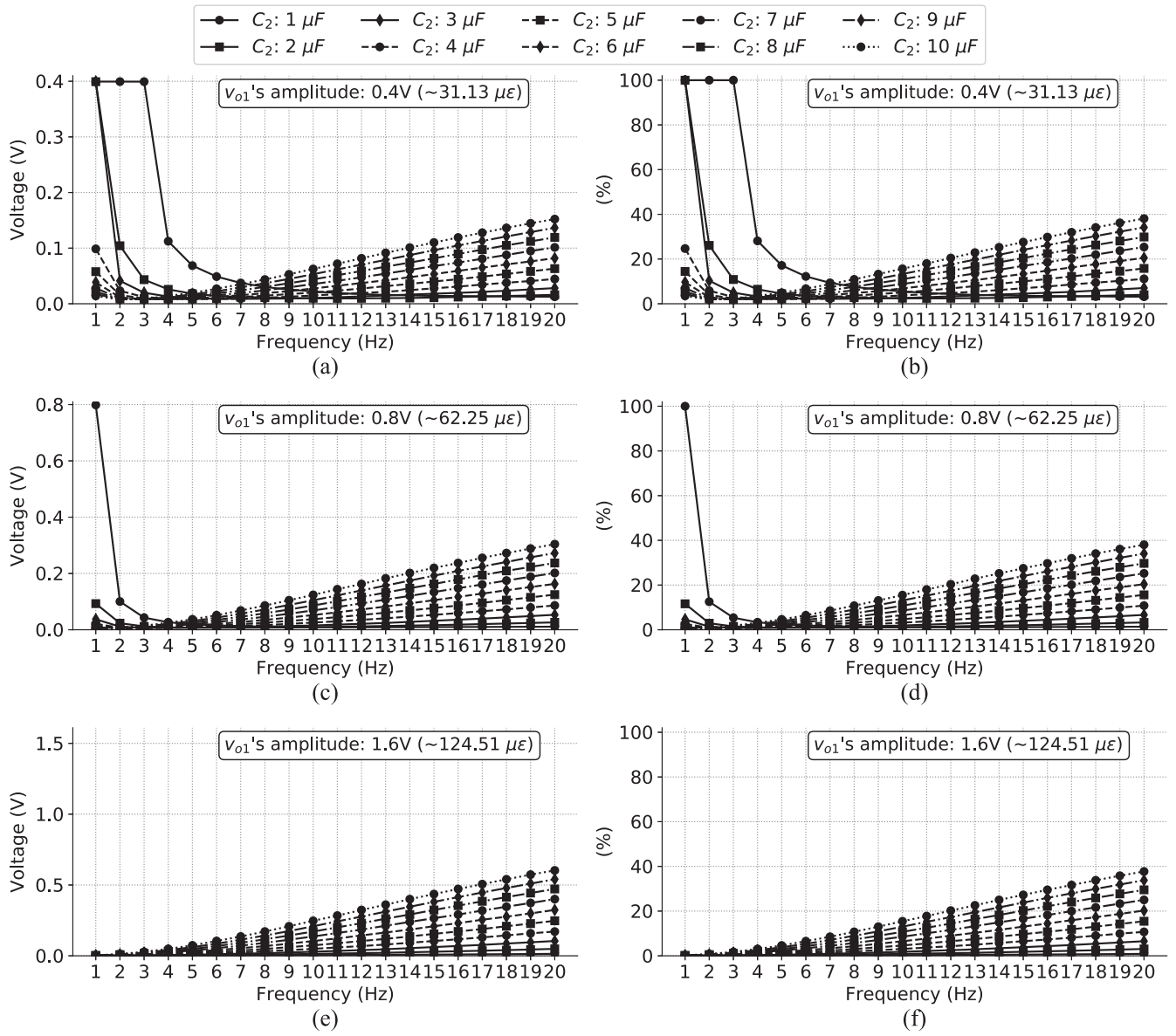

Figure 5. Measurement error when varying C_2: (a), (c), (e) absolute and (b), (d), (f) percentage difference. R_3 is set to 47 $k\Omega$. Conversion to strain units is done considering C_1 equal to 2.5 nF.

Table 1. Capacitor C_2 selection: simulated capacitor sizes and related cut-off frequency, for R_5 equal to 1 $k\Omega$.

C_2 (μF)	f_l^F (Hz)	C_2 (μF)	f_l^F (Hz)
1	159.15	6	26.53
2	79.58	7	22.74
3	53.05	8	19.89
4	39.79	9	17.68
5	31.83	10	15.92

transient simulations with Tina-TI by Texas Instruments and DesignSoft, a SPICE-based simulation tool designed to build and simulate analogue circuits.

We first study the effect of having different R_5C_2 delay network configurations. For the sake of brevity, we will only show the results for different capacitor sizes, from 1 to 10 μF, while the rest of circuit parameters including R_5 remain fixed. The applied input signal v_{o1} is sinusoidal with varying amplitude $A_{v_{o1}}$, from 0.2 to 1.6 V in individual steps of 0.2 V, and frequency $f_{v_{o1}}$, from 1 to 20 Hz, in 1 Hz steps. The selected amplitudes were chosen to match the ADC input range (it is worth remarking that the zero of the circuit is shifted to the middle of the ADC input range, using a reference of $V_{cc}/2$), whereas the selected frequencies cover the range of frequencies of interest for typical applications of fatigue damage monitoring.

In figure 5 we plot the average *absolute* and *relative* measurement error, defined as the average absolute (in Volts) and the percentage difference between the peak/trough amplitudes when post processing v_{o1} with both a standard peak-trough detection software algorithm, and with our hardware-based peak-trough detector circuit. Since our hardware is simulated, the latter are obtained using a post-

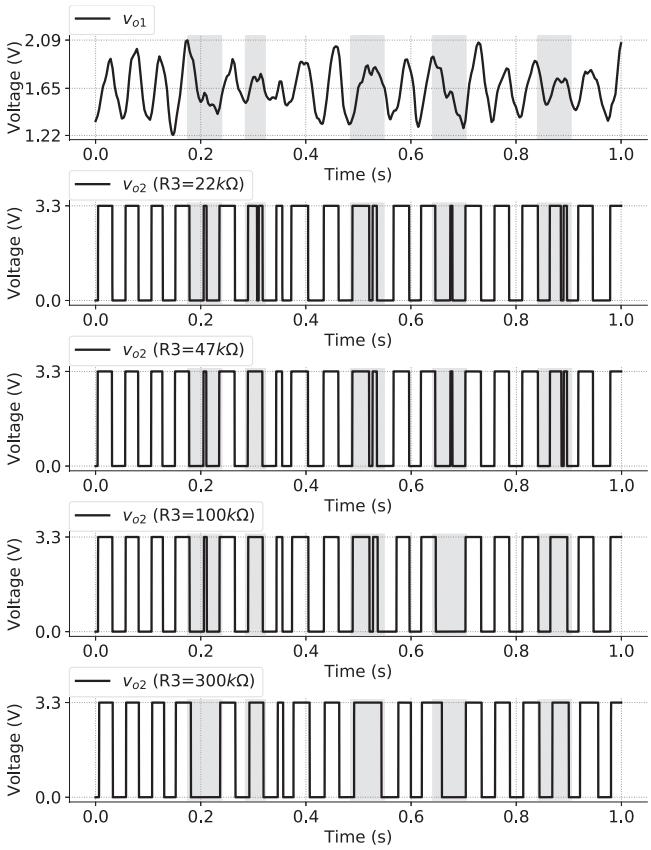

Figure 6. Measurement error when varying R_3. R_4, R_5 and C_2 are 10 $M\Omega$, 1 $k\Omega$ and 5 μF, respectively.

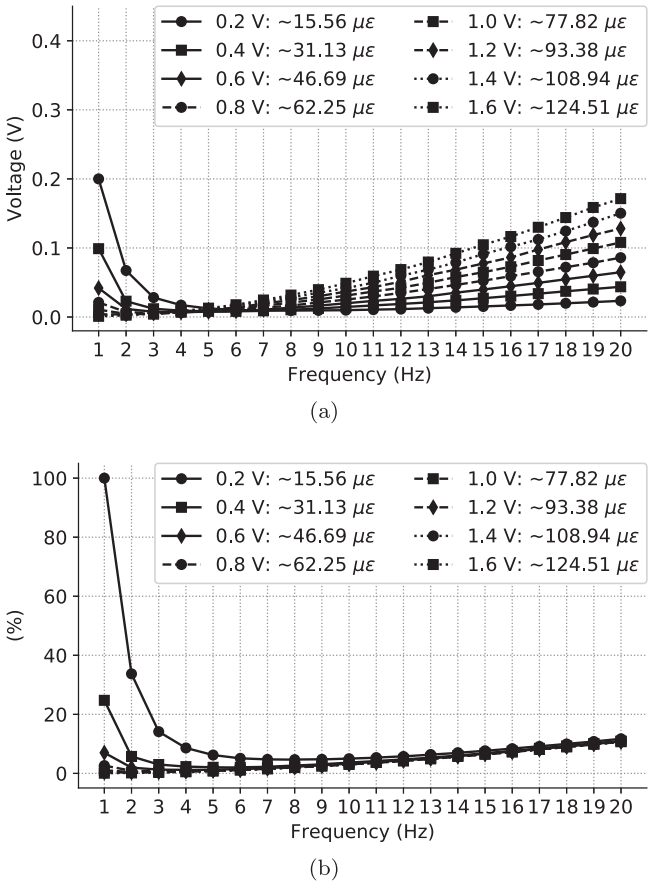

Figure 7. Measurement error when varying the voltage amplitude of v_{o1}: (a) absolute and (b) percentage difference. C_1, C_2 and R_3 are set to 2.5 nF, 4 μF, and 47 $k\Omega$, respectively.

processing algorithm that computes peaks and troughs from the simulated values of v_{o2} and v_{o1}^{ϕ} signals as output from Tina-TI simulator. These results represent a best-case performance in real-world deployments since other factors such as interrupt latency and the latency and settling time of the ADC are not captured.

In the first instance, the measurement error increases almost linearly with frequency as the capacitor size is increased. This behaviour is expected of an RC delay circuit —given a fixed resistance R_5, the bigger the capacitance C_2, the smaller the cut-off frequency f_l^F of the circuit (see table 1), and consequently, the more attenuated the amplitude of v_{o1}^{ϕ} becomes as $f_{v_{o1}}$ approaches f_l^F. It is to be noted that the signal to be sampled, v_{o3}, is v_{o1}^{ϕ} after a voltage follower and another series RC network with a much higher low cut-off frequencyhence with no significant influence over v_{o1}^{ϕ} for the range of frequencies of interest. Therefore, the detection error at higher $f_{v_{o1}}$ is effectively due to the fact that the system is sampling a signal whose amplitude has been lowered because of the proximity of $f_{v_{o1}}$ to f_l^F.

A priori, it appears that smaller capacitor sizes, e.g. of the order of 2–5 μF allow only measurement over a wider range of frequencies with relatively low error. However, one problem that is encountered is that for small input signals (low amplitude and low frequency), which may be of monitoring interest, the Schmitt trigger toggles at an undesired value or does not toggle at all. The reason for this has been found to be related to the hysteresis of the circuit, as illustrated in the simulation results of figure 6. The peak detector is driven with a synthetically generated input signal v_{o1} which may reflect a typically encountered strain signal on a real application. In this case, different R_3 values are evaluated while all remaining circuit parameters are fixed. It can be observed that for certain small amplitude signal variations the Schmitt trigger stops toggling as R_3 is increased. The figure also depicts the case where the hysteresis is too high (for R_3 equal to 300 $k\Omega$) and the circuit fails in accurately toggling at the right peak or trough.

The final set of simulation experiments considers that all circuit parameters are fixed. This implies that the circuit performance will only depend on the amplitude and frequency of the input signal. Similarly to the previous experiments, we consider different voltage amplitudes and oscillation frequencies. The results are plotted in figure 7, which presents the same variation of measurement error with increasing frequency as discussed above. It also shows that the variation in relative measurement error is proportional to the amplitude of the applied input signal, which could be useful for calibration and data post-processing purposes.

4.2. Validation on real hardware

Next, we describe the experimental procedure used in our validation, followed by a discussion on the performance evaluation results for our system.

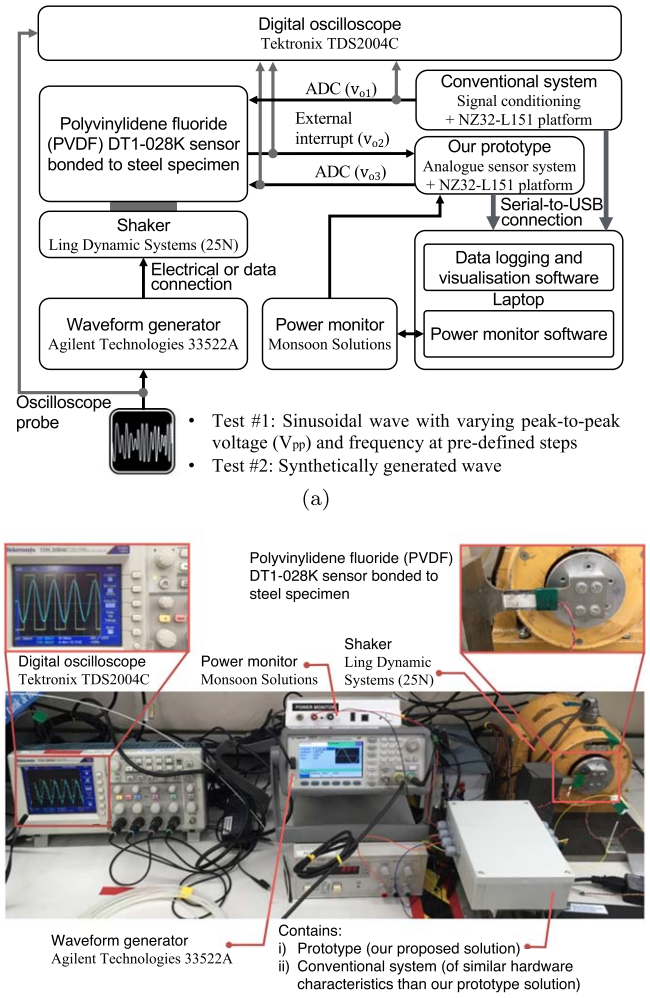

Figure 8. Laboratory experimental setup: (a) schematics and (b) photo of the experimental setup.

Table 2. Components and circuit parameters of the analogue sensor system prototype.

Parameter	Value	Parameter	Value
Op-amp (OA1)	LPV811	R_5,R_7	1 kΩ
Op-amp (OA2/3)	OPA2333	R_6	50 Ω
V_{cc}	3.3 V	R_8,R_9	10 kΩ
V_{ee}	0 V	C_1	4 nF
R_1,R_3	47 kΩ	C_2	4 μF
R_2	1 GΩ	C_3	2 μF
R_4	10 MΩ		

4.2.1. Laboratory experimental setup. Figure 8(a) illustrates the experimental procedure, whereas figure 8(b) shows a picture of the experimental setup. A prototype of the analogue sensor system was assembled on a solderless breadboard with the electrical scheme of figures 3(a) and 4(a), and connected to a *NZ32-L151* device using the ADC channel 0 (*PA0-WKUP1* pin) and GPIO line 1 (*PA1* pin) for v_{o2} and v_{o3} signals, respectively. Table 2 lists the components and circuit parameters of the prototype. The *NZ32-L151* device is

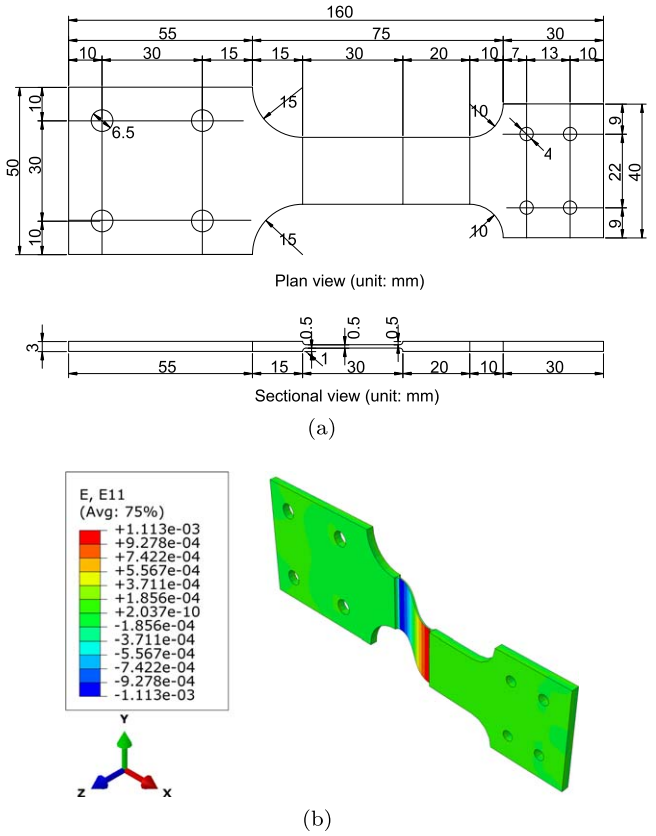

Figure 9. Test specimen used for laboratory experiments: (a) dimensions (mm); (b) modelling of strain distribution across the specimen using Abaqus version 6.12 [53].

programmed with a specific application developed in the Contiki OS and based on the software architecture described in subsection 3.3. However, for these experiments, RF transmissions are disabled. In addition, the *NZ32-L151* device sends all the ADC readings as well as the output of the rainflow cycle counting algorithm to a laptop via a serial-to-usb connection. All the arriving data at the laptop are timestamped and logged on files for later data analysis. It is worth remarking that this is for evaluation purposes; in a real-world application, only strain-cycle information would be transmitted.

For comparison, an alternative prototype, representing a conventional system was created utilizing the same signal conditioning block from our previous setup. The output signal v_{o1} is passed through an additional op-amp in a voltage follower configuration followed by a low-pass RC filter (of similar R_7/C_3 values), and its output connected to the ADC channel 0 of a separate *NZ32-L151* device. This device is programmed with specific application software that has also been developed in Contiki OS and which takes samples continuously at a sampling frequency of 64 Hz. All the sampled data is stored in a temporal buffer and later pre-processed using a C-based implementation of a typical peak-trough detection algorithm [51] prior to executing our implementation of the rainflow cycle counting algorithm. Similarly, all the obtained ADC readings as well as the output

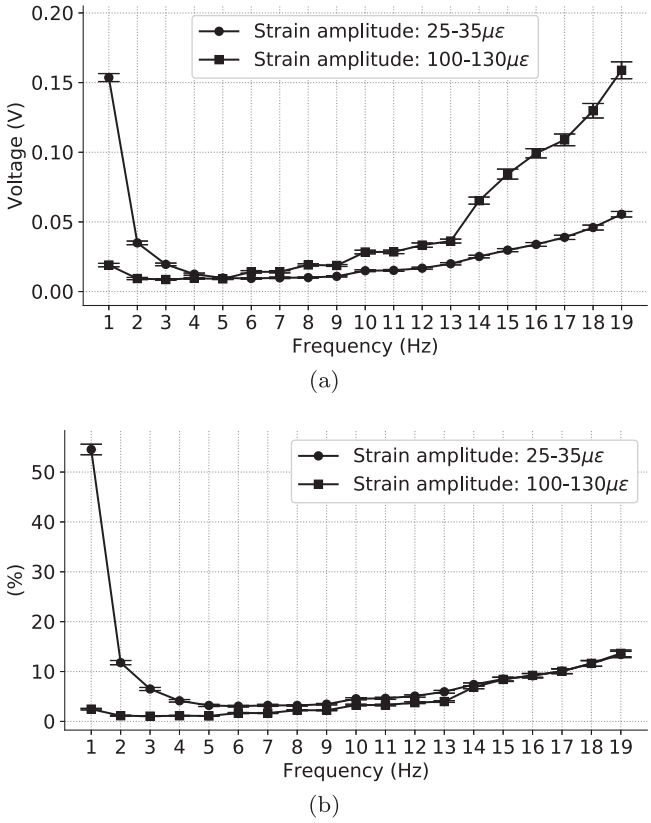

Figure 10. Experimental results: average (a) absolute and (b) relative measurement error. The error bars denote 95% confidence intervals.

of both algorithms are sent to a laptop for further data analysis.

Both prototypes are connected to a single PVDF DT1-028K sensor [36]. The sensor is bonded onto the surface of a dog-bone shaped steel specimen (mild steel EN 3B) using a cyanoacrylate-based (super glue) adhesive. The specimen, whose geometric characteristics are given in figure 9(a), has been specifically manufactured for fatigue testing and its design is specified to reduce the residual stress and work-hardening. Figure 9(b) shows the distribution of longitudinal strain (along x axis) of the specimen with 1 mm of displacement in the shaker. As shown in the figure 8(b), the specimen is both fixed onto a steel beam with base attached to the laboratory bench as well as onto a vibration shaker system. An Agilent 33522A waveform generator is used to drive the shaker while a digital oscilloscope records the signal outputs from v_{o1}, v_{o2} and v_{o3}. Finally power consumption measurements of each individual prototype were performed using a power monitor from Monsoon Solutions [52]. Power consumption results are given later in section 4.2.3.

4.2.2. Performance results under sinusoidal excitation. The performance of the analogue peak-trough detection was first characterised under varying sinusoidal excitation. Following a similar procedure as in our simulations, a series of driving waveforms, each with a different peak-to-peak voltage (V_{pp}) and oscillation frequency, were generated by the signal generator in turn. We chose V_{pp} to be 600 mV and 1.6 V, which yielded strain amplitudes of approximately 25–35 $\mu\varepsilon$ and 100–130 $\mu\varepsilon$ depending on the signal frequency. For each V_{pp}, the frequency was varied from 1 to 20 Hz, in steps of 1 Hz. For each setting, data generated by both prototypes were recorded for over 1 min and later analysed to show the average absolute and relative measurement error between them.

Results are depicted in figure 10. It can be seen that both experimental and simulation results are in good agreement with each other, which help us validate and benchmark our design. It is also worth noting that our proposed system seemed to reach its performance limit at the frequency of 20 Hz. In investigating this issue further, it was found that the latency that is introduced in transferring the sampled data to the laptop caused an unintended behaviour in our system. This was to have been expected since our system operates using hardware interrupts whereas operations such data transfer via serial are known to be non-re-entrant and non-thread-safe when used in a real-time OS. Due to the difficulty of accurately synchronising both prototype systems, we have disregarded the computation of the measurement error at such frequency for figure 10.

While previous experimental work provides a framework to quantify the performance of our peak-trough detector, the goal of this experiment is to evaluate the performance and applicability of our entire system in a reasonably realistic scenario. We illustrate this by comparing the number of strain cycles that are captured by both approaches over a sufficiently long period of time. In order to do so, the vibration shaker system is driven with the synthetically generated signal of figure 11(a) for a total duration of 2 hours. The distribution of signal frequencies over time is shown by way of the short-time Fourier transform (STFT) in figure 11(b). The circuit parameters from the previous setup remain the same (see table 2). It is worth noting that the strain cycle data captured by our system can immediately be plotted (only conversion from voltage to strain units is necessary). For the conventional method, the experimental procedure has been to collect all sampled data as in previous experiments and post-processing them using a peak-trough detection algorithm followed by our implementation of the rainflow cycle counting algorithm. For both systems, the latter has been configured with a buffer size N_S equal to 256, although no significant variation was found with other sizes.

Histograms of full strain cycles versus strain range obtained by both systems are plotted in figure 11(c). The number of half cycles was very small for both systems and is therefore not presented here for the sake of brevity. A comprehensive comparative analysis of these data, along with a fatigue test-bed study that seeks to predict the level of damage and the closeness to failure of a similar test specimen using our sensor solution, is the subject of ongoing work.

Figure 11(c) shows a good agreement between the histograms of full cycles for both systems. It can be seen that for strain ranges bigger than 140 $\mu\varepsilon$ our system progressively reports smaller numbers of full cycles or does not report any values. This difference is due to the peak-trough measurement error that our system has with respect to the conventional approach. As suggested at the end of section 4.1, it could be

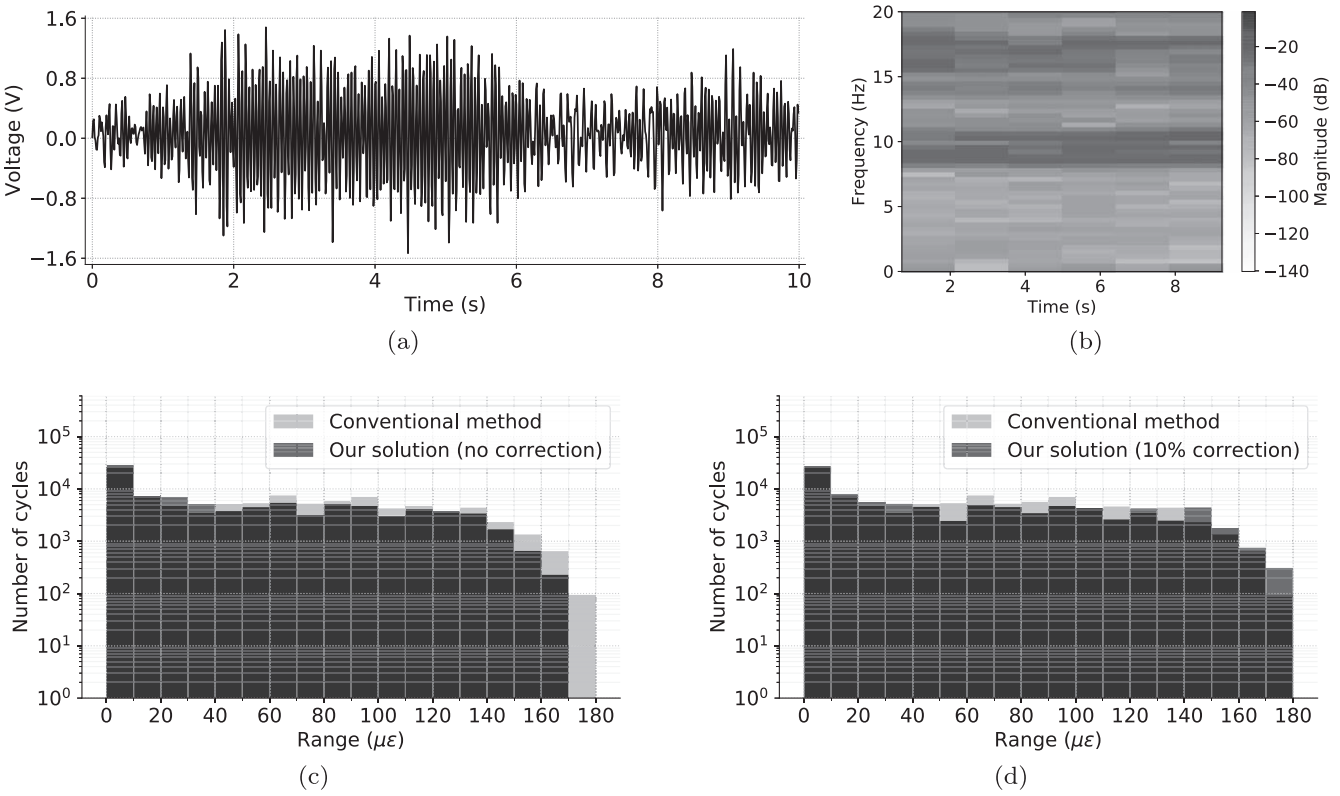

Figure 11. Rainflow cycle counting performance: (a) synthetically generated input signal and (b) its distribution of frequencies over time; full cycle histograms over a 2 h test (c) with no measurement error correction and (d) with a 10% error correction applied over all strain range values. The bin size is 10 $\mu\varepsilon$.

possible to apply a data correction factor on the strain cycle data (thus accounting for any peak-trough measurement errors) given prior knowledge of the signal frequencies that will be encountered at the location where the sensor is being installed. In practical applications—and not exclusive to fatigue monitoring—such knowledge is usually obtained prior to installation of any sensing instrumentation [25], therefore it is possible to obtain similar results as if using the conventional approach of fatigue measurement. This is demonstrated in figure 11(d), where a simple correction factor of +10% strain range has been chosen and linearly applied to the data. Equivalently, this factor means that a + 5% increase in strain amplitude is applied to peaks and troughs, according to our previous simulation and experimental study.

4.2.3. Power profiling. Power consumption measurements were obtained for each prototype individually. Because our solution is not exclusively intended for use with LoRa/LoRaWAN, for these experiments the LoRa transceiver is turned off and therefore no power consumed in LoRa/LoRaWAN transmissions are captured by our measurements. We refer to Casals *et al* [54] for a comprehensive power consumption study of LoRa and LoRaWAN for several transceiver and protocol settings, which include the spreading factor, coding rate, the duration of reception windows and the number of retransmission attempts.

Figure 12(a) shows a snapshot of the instantaneous consumption for different oscillation frequencies of the sinusoidal input signal generated with the oscilloscope, whereas figure 12(b) presents the average results. The latter figure also includes an estimation of battery life considering a single 19 Ah-3.6 V lithium battery (although we consider sustained operation at 3.3 V). We chose this battery based on our previous experience with WSN deployments in the civil engineering field [25, 55, 56]. As observed, the improvement concerning power consumption is correlated to a reduction in the computational workload of the MCU, which allows it to switch to low-power saving mode in between consecutive hardware interrupts. This boosts the operational lifetime of our proposed system as much as a factor of 9 (approximately up to 2 years of operation) as compared to the conventional approach.

Finally, the experimental average power consumption of our analogue sensor system when disconnected from the *NZ32-L151* platform is 0.58 mW, approximately eight times smaller than our reported system power consumption. This suggests that the overall power consumption of the entire prototype including the wireless platform and the analogue sensor system could be further reduced with hardware and software improvements in the wireless platform in use.

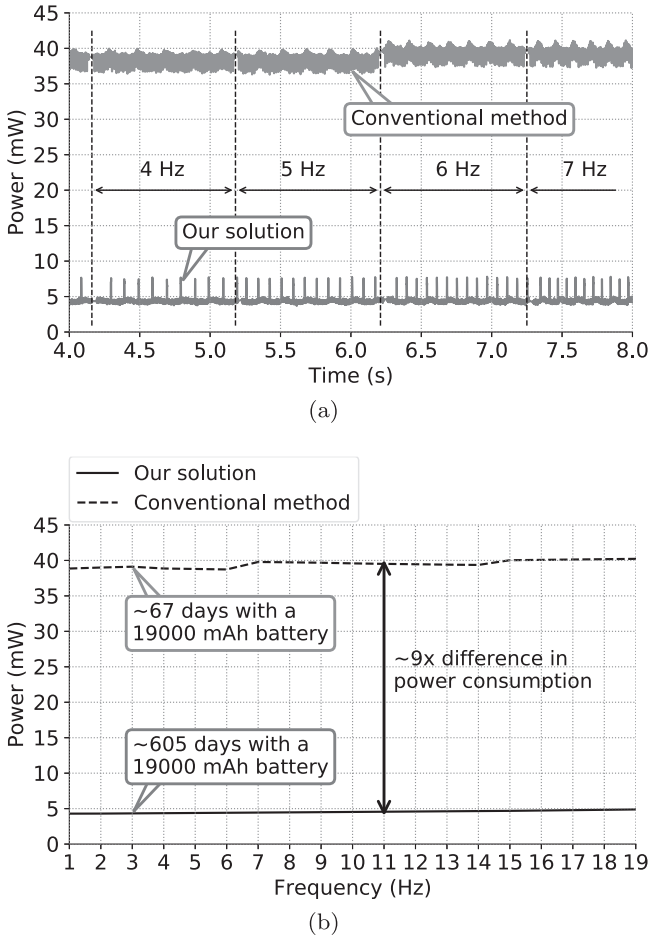

Figure 12. Power consumption: (a) one second snapshot of instant consumption at different excitation frequencies. Spikes in the data obtained with our solution are the interrupt triggers for sampling of peaks and troughs. (b) Average results. The conventional approach has an average power consumption of 40 mW, while our proposed solution achieves up to 5 mW on average.

5. Conclusions

This paper proposes a potential solution to deploy WSNs for long-term fatigue life assessment of civil engineering structures, which uses a power-efficient design of a LoRa-based embedded sensor system having the ability to measure fatigue strain cycles in a continuous manner. At the core of our design is a hardware module which uses analogue electronics to condition and find both peaks and troughs of a strain signal measured with a piezoelectric sensor. Peaks and troughs are signalled by way of hardware interrupts to the MCU, which is configured to remain in low-power mode most of the time to efficiently reduce overall power consumption. The MCU then wakes up and triggers a single ADC measurement corresponding to the voltage level of the signalled peak or trough. These measurements are processed locally using the rainflow cycle counting algorithm, a standard method for counting fatigue strain cycles. With appropriate hardware parameter settings, our design provides a power-efficient alternative to the conventional approach for fatigue strain-cycle measurement, which requires continuous acquisition of strain data with a high sampling rate, followed by data pre-processing using standard peak-trough detection algorithms before actual strain-cycle measurement. Extensive computer simulation and laboratory experiments showed good agreement between the strain-cycle histograms obtained for both our system and an embedded prototype of similar hardware and software characteristics that was built based on the conventional approach. Our proposed solution achieved a 9× reduction in power consumption thereby enabling almost up to two years of continuous operation on a single battery. Therefore, our proposed solution proves to be promising to be applied in real-world civil engineering deployments. For our immediate future research, we plan to perform a comprehensive long-term fatigue study both in the laboratory, and through the placement of a large number of wireless sensor devices based on our design on a real structure.

Acknowledgments

This research has been made possible through the Innovation and Knowledge Centre for Smart Infrastructure and Construction (CSIC) funded by EPSRC (EP/N021614/1) and Innovate UK (920035). The authors would like to thank Dr Tzu-Hsuan Lin of National Central University (Taiwan) for his input on signal conditioning of piezoelectric film sensors and Dr Seiji Yamada of the Japan Railway Technical Research Institute for his input on fatigue sensing. The authors are also grateful to Mr Peter Knott and Mr Alistair Ross of the University of Cambridge for their valuable support in setting up the laboratory test bed.

ORCID iDs

David Rodenas-Herráiz https://orcid.org/0000-0001-6156-5580
Xiaomin Xu https://orcid.org/0000-0002-1255-9026
Paul R A Fidler https://orcid.org/0000-0003-4594-4323

References

[1] Suresh S 1998 *Fatigue of Materials* 2nd edn (Cambridge: Cambridge University Press)
[2] Bannantine J A, Comer J J and Handrock J L 1990 *Fundamentals of Metal Fatigue Analysis* (Englewood Cliffs, NJ: Prentice Hall)
[3] Ye X W, Su Y H and Han J P 2014 A state-of-the-art review on fatigue life assessment of steel bridges *Math. Problems Eng.* **2014** 1–13
[4] Zhou Y, Dawood M and Gencturk B 2017 High-cycle fatigue performance of high-mast illumination pole bases with pre-existing cracks *J. Constr. Steel Res.* **138** 463–72
[5] Wieghaus K T, Mander J B and Hurlebaus S 2017 Damage avoidance solution to mitigate wind-induced fatigue in steel traffic support structures *J. Constr. Steel Res.* **138** 298–307
[6] Ihn J-B and Chang F-K 2004 Detection and monitoring of hidden fatigue crack growth using a built-in piezoelectric sensor/actuator network: I. Diagnostics *Smart Mater. Struct.* **13** 609–20

[7] Bai S, Li X, Xie Z, Zhou Z and Ou J 2014 A wireless fatigue monitoring system utilizing a bio-inspired tree ring data tracking technique *Sensors* **14** 4364–83

[8] Feltrin G, Popovic N, Flouri K and Pietrzak P 2016 A wireless sensor network with enhanced power efficiency and embedded strain cycle identification for fatigue monitoring of railway bridges *J. Sens.* **2016** 1–14

[9] Alavi A H, Hasni H, Lajnef N, Chatti K and Faridazar F 2016 An intelligent structural damage detection approach based on self-powered wireless sensor data *Autom. Constr.* **62** 24–44

[10] Alavi A H, Hasni H, Lajnef N, Chatti K and Faridazar F 2016 Damage detection using self-powered wireless sensor data: an evolutionary approach *Measurement* **82** 254–83

[11] Alavi A H, Hasni H, Jiao P, Borchani W and Lajnef N 2017 Fatigue cracking detection in steel bridge girders through a self-powered sensing concept *J. Constr. Steel Res.* **128** 19–38

[12] Popovic N, Feltrin G, Jalsan K-E and Wojtera M 2017 Event-driven strain cycle monitoring of railway bridges using a wireless sensor network with sentinel nodes *Struct. Control Health Monit.* **24** e1934

[13] Liu P, Lim H J, Yang S, Sohn H, Lee C H, Yi Y, Kim D, Jung J and Bae I-H 2017 Development of a 'stick-and-detect' wireless sensor node for fatigue crack detection *Struct. Health Monit.* **16** 153–63

[14] Dorafshan S, Thomas R J and Maguire M 2018 Fatigue crack detection using unmanned aerial systems in fracture critical inspection of steel bridges *J. Bridge Eng.* **23** 04018078

[15] Kong X, Li J, Bennett C, Collins W, Laflamme S and Jo H 2019 Thin-film sensor for fatigue crack sensing and monitoring in steel bridges under varying crack propagation rates and random traffic loads *J. Aerosp. Eng.* **32** 04018116

[16] Infrastructure and Capital Investment Committee 2016 *Inquiry into the circumstances surrounding the closure of the Forth Road Bridge 4* Scottish Parliamentary Corporate Body https://www.parliament.scot/parliamentarybusiness/CurrentCommittees/97411.aspx

[17] National Infrastructure Commission, Data for the Public Good, Technical report: https://nic.org.uk/publications/data-public-good/, 2017, [Accessed 12 April 2019]

[18] Yao Y, Tung S-T E and Glisic B 2014 Crack detection and characterization techniques—an overview *Struct. Control Health Monit.* **21** 1387–413

[19] Achenbach J D 2000 Quantitative nondestructive evaluation *Int. J. Solids Struct.* **37** 13–27

[20] Johnson M B, Ozevin D, Washer G A, Ono K, Gostautas R S and Tamutus T A 2012 Acoustic emission method for real-time detection of steel fatigue crack in eyebar *Transp. Res. Rec.: J. Transp. Res. Board* **2313** 72–9

[21] Zhang Y 2006 *In situ* fatigue crack detection using piezoelectric paint sensor *J. Intell. Mater. Syst. Struct.* **17** 843–52

[22] Mršnik M, Slavič J and Boltežar M 2013 Frequency-domain methods for a vibration-fatigue-life estimation—application to real data *Int. J. Fatigue* **47** 8–17

[23] Marzbanrad B, Jahed H and Toyserkani E 2016 On the sensitivity and repeatability of fiber Bragg grating sensors used in strain and material degradation measurement of magnesium alloys under cyclic loads *Int. J. Adv. Manuf. Technol.* **86** 3453–61

[24] Kong X and Li J 2018 Vision-based fatigue crack detection of steel structures using video feature tracking *Comput.-Aided Civ. Infrastruct. Eng.* **33** 783–99

[25] Rodenas-Herráiz D, Soga K, Fidler P and de Battista N 2016 *Wireless Sensor Networks for Civil Infrastructure Monitoring—A Best Practice Guide* (London, UK: ICE Publishing) (https://doi.org/10.1680/wsncim.61514)

[26] Sirohi J and Chopra I 2000 Fundamental understanding of piezoelectric strain sensors *J. Intell. Mater. Syst. Struct.* **11** 246–57

[27] ASTM E1049-85 2017 Standard practices for cycle counting in fatigue analysis *American Society for Testing And Materials (ASTM) International* vol 85https://www.astm.org/Standards/E1049

[28] Al-Fuqaha A, Guizani M, Mohammadi M, Aledhari M and Ayyash M 2015 Internet of things: a survey on enabling technologies, protocols, and applications *IEEE Commun. Surv. Tutorials* **17** 2347–76

[29] Alavi A H, Hasni H, Lajnef N and Chatti K 2016 Continuous health monitoring of pavement systems using smart sensing technology *Constr. Build. Mater.* **114** 719–36

[30] Miner M A 1945 Cumulative fatigue damage *J. Appl. Mech.* **12** A159–64

[31] BS EN 1993-1-9:2005—Eurocode 3. Design of steel structures. Fatigue, British Standards Institution, 2005.

[32] Load and Resistance Factor Design (LRFD) Bridge Design Specifications—SI Units, American Association of State Highway and Transportation Officials (AASHTO), 8 edn., 2017.

[33] LoRa Alliance Technical Committee, LoRaWAN™ 1.1 Specification, LoRa Alliance, 2017.

[34] Wang Y-P E, Lin X, Adhikary A, Grovlen A, Sui Y, Blankenship Y, Bergman J and Razaghi H S 2017 A primer on 3GPP narrowband internet of things *IEEE Commun. Mag.* **55** 117–23

[35] Ouyang X, Dobre O A, Guan Y L and Zhao J 2017 Chirp spread spectrum toward the nyquist signaling rate—orthogonality condition and applications *IEEE Signal Process Lett.* **24** 1488–92

[36] TE Connectivity, Piezoelectric Sensors, http://te.com/usa-en/products/sensors/piezo-film-sensors.html, [Accessed 12 April 2019].

[37] ANSI/IEEE Std 176-1987, *IEEE Standard on Piezoelectricity*, 1988

[38] Modtronix Engineering, NZ32-SC151 breakout board, http://wiki.modtronix.com/doku.php?id=products:nz-stm32:nz32-sc151, [Accessed 12 April 2019]

[39] Measurement Specialties, Piezo Film Sensors—Technical Manual, https://strainsense.co.uk/wp-content/uploads/2017/08/Piezo_Technical_Manual.pdf, 2008, [Accessed 12 April 2019]

[40] Texas Instruments, LPV811: Single Channel 450 nA Precision Nanopower Operational Amplifier, http://ti.com/product/LPV811, [Accessed 12 April 2019]

[41] Analog Devices, CN-0350: 12-Bit, 1 MSPS, Single-Supply, Two-Chip Data Acquisition System for Piezoelectric Sensors, http://analog.com/en/design-center/reference-designs/hardware-reference-design/circuits-from-the-lab/cn0350.html, [Accessed 12 April 2019]

[42] Texas Instruments, OPA2333: 1.8 V, 17 μA, 2 channels, microPower, Precision, Zero Drift CMOS Op Amp, http://ti.com/product/OPA2333, [Accessed 12 April 2019]

[43] Chaniotakis M and Cory D 2006 *Operational Amplifier Circuits Comparators and Positive Feedback* (MIT Open Courseware)

[44] Sedra A S and Smith K C 2015 *Microelectronic Circuits, The Oxford Series in Electrical and Computer Engineering* 7 edn (New York: Oxford University Press)

[45] Dunkels A, Grönvall B and Voigt T 2004 Contiki—a lightweight and flexible operating system for tiny networked sensors *Proc. 29th Annual IEEE Int. Conf. on Local Computer Networks, LCN 2004* (Tampa, Florida, USA: IEEE Computer Society) pp 455–62

[46] The freertos kernel, http://freertos.org/, [Accessed 12 April 2019]

[47] Semtech Corporation, LoRaWAN endpoint stack implementation and example projects, https://github.com/Lora-net/LoRaMac-node, [Accessed 12 April 2019]
[48] Source code, simulation and data analysis scripts, and relevant data, https://bitbucket.org/csic-wifat/csic-wireless-fatigue-sensor-system/src/master/ (also https://doi.org/10.17863/CAM.40017), [Accessed 20 May 2019]
[49] STMicroelectronics, STM32L151/152, https://st.com/en/microcontrollers-microprocessors/stm32l151-152.html, 2017, [Accessed 12 April 2019]
[50] Bor M C and Roedig U 2017 LoRa transmission parameter selection *Proc. 13th Int. Conf. on Distributed Computing in Sensor Systems, DCOSS* (Ottawa, ON: IEEE) pp 27–34
[51] H Xu, peakdetect: Peak detection in a wave, https://github.com/xuphys/peakdetect, 2013, [Accessed 12 April 2019]
[52] Monsoon Solutions, http://msoon.com/, [Accessed 12 April 2019]
[53] Dassault Systèmes, Abaqus Unified FEA, https://3ds.com/products-services/simulia/products/abaqus/, [Accessed 12 April 2019].
[54] Casals L, Mir B, Vidal R and Gomez C 2017 Modeling the energy performance of LoRaWAN *Sensors* **17** 2364
[55] Nawaz S, Xu X, Rodenas-Herráiz D, Fidler P R A, Soga K and Mascolo C 2015 Monitoring a large construction site using wireless sensor networks *Proc. 6th ACM Workshop on Real World Wireless Sensor Networks, RealWSN '15* (Seoul, South Korea: ACM) pp 27–30
[56] Xu X, Soga K, Nawaz S, Moss N, Bowers K and Gajia M 2015 Performance monitoring of timber structures in underground construction using wireless SmartPlank *Smart Struct. Syst.* **15** 769–85